nature astronomy

LETTERS

https://doi.org/10.1038/s41550-022-01669-0

Conditions for aeolian transport in the Solar System

Andrew Gunn[1,2] **and Douglas J. Jerolmack**[2,3] ✉

Sand dunes, which arise wherever loose sediment is mobilized by winds that exceed threshold speed and grains are sufficiently strong to survive collisions[1], are ubiquitous in the Solar System[2]. However, current threshold theories usually neglect physical processes that become relevant under exotic conditions[3,4], and are in disagreement when extrapolated to extraterrestrial planetary bodies[5-9]. Here we draw on results in contact[10], rarefied gas[11], statistical[12] and adhesion[13] mechanics to present a theory for the fluid and impact thresholds of aeolian transport that encompasses the various conditions present in Solar System bodies. Our theoretical predictions are consistent with available experimental threshold observations and indicate that these thresholds strongly depend on local environmental conditions everywhere but Earth. Our results suggest, among other things, that Titan's dunes are locally sourced[4] and that Mars's high threshold makes its dunes more resistant to motion[14]. This work highlights the role of dunes in understanding atmospheric dynamics and surface sediment. Further studies are needed to include hitherto neglected and still poorly understood processes.

We have developed theories to find the two threshold friction velocities u_* that must be exceeded by wind to move sand and form dunes: the 'fluid' threshold, the wind required to move a particle from rest; and the 'impact' threshold, the minimum wind to maintain steady saltation. Mass transport scales in excess of the latter, whereas saltation must start from the former[7]. This is done from first principles, and by employing more stringent or recent results from aeronautics and contact mechanics that are not typically considered in aeolian studies (Methods). Each theory has a single physically meaningful free parameter, which is found by fitting to a newly compiled comprehensive data set. Using these theories, we provide revised predictions of the thresholds across the Solar System where dunes are known to exist (Fig. 1a–f), paying special attention to the range of environmental conditions on each planetary body.

The fluid threshold of motion is defined by a balance between the forces retaining a grain that is resting in a pocket on a bed of grains, and the forces that can remove it from this pocket[8]. Weight and adhesion forces correspond to the former, while drag and buoyancy to the latter. The lift force can act to retain or remove the grain, depending on shear and fluid properties (Fig. 1h). These forces all have functional forms constrained from theory, apart from the lift and drag forces, where we employ refined empirical predictions for the respective coefficients. The complete torque balance in a fragile pocket geometry reads $r_\mathrm{G}F_\mathrm{G}+r_\mathrm{A}F_\mathrm{A}=r_\mathrm{D}F_\mathrm{D}+r_\mathrm{L}F_\mathrm{L}+r_\mathrm{B}F_\mathrm{B}$, where the moments and forces are defined graphically in Fig. 1g. Expanding and non-dimensionalizing this equation (Methods), we can write the fluid threshold of motion as the sum of two fractions that are equal to unity,

$$1=\frac{\alpha}{\Theta_\mathrm{p}}+\frac{\beta}{\Phi_\mathrm{p}},\qquad(1)$$

where α and β depend on geometry and the drag and lift coefficients, and Θ_p and Φ_p depend on fluid and solid properties. The Shields-like number $\Theta_\mathrm{p}\propto 1/d$ non-dimensionalizes the fluid speed at the particle centre, u_p, using the submerged particle weight, whereas u_p is non-dimensionalized in $\Phi_\mathrm{p}\propto d$ by the adhesion due to grain-surface energy, γ (Methods). Noting the scaling of these parameters with grain diameter, d, it is clear that for small particles the threshold tends toward $\Phi_\mathrm{p}=\beta$, and for large particles $\Theta_\mathrm{p}=\alpha$. The crossover between these limiting behaviours, where winds must overcome adhesion or weight, respectively, depends on all parameters. As an example, for typical quartz grains on Earth this transition occurs for a grain size of roughly 40 µm; hence, dune sands are little affected by adhesion, while dust grains are strongly affected. This may not, however, be the case on other planets.

There is one unaccounted-for constant required to close the solution for the fluid threshold: the ratio of the characteristic length-scale between particles in contact, d_0, and roughness at the contact scale[13] (Fig. 1i). Assuming that this ratio, $\mathcal{B}$, is approximately universal for natural sand grains, we determine it to be $\mathcal{B}\approx 8.74$ by fitting the theory to wind-tunnel and field measurements of the fluid threshold (Methods). This allows prediction of the fluid threshold on each planetary body of interest, if the dimensionless parameters α, β, Θ_p and Φ_p are known. Our formulation builds on previous hydrodynamic approaches[8,15] (Supplementary Section 1), with the following improvements: it accounts for the lift and adhesion forces explicitly, improves the parameterizations for the lift and drag coefficients[11,16] and has just one free parameter that is specific to sediment transport.

Using well established theory on the behaviour of gases[12] (Methods), observations of temperature and pressure, and measured material constants (Supplementary Table 1), we find that the predicted fluid entrainment threshold spans three orders of magnitude for reasonable grain diameters across the Solar System (Fig. 2a). To first order, this range is controlled by fluid kinematic viscosity (Extended Data Fig. 1). We see that both particle composition, and variability in pressure and temperature, can lead to a wide range of threshold wind speeds on a given planetary body—with the exception of Earth, where these parameters vary little. These predictions are mostly higher than alternative theories[8,9], while being similarly accurate when compared with experimental data (Extended Data Figs. 2 and 3). The sensitivity of drag pressure to wind stress—that is, the drag coefficient, C_D—varies greatly across these environments, depending

---

[1]School of Earth, Atmosphere and Environment, Monash University, Clayton, Victoria, Australia. [2]Department of Earth and Environmental Sciences, University of Pennsylvania, Philadelphia, PA, USA. [3]Department of Mechanical Engineering and Applied Mechanics, University of Pennsylvania, Philadelphia, PA, USA. ✉e-mail: sediment@sas.upenn.edu

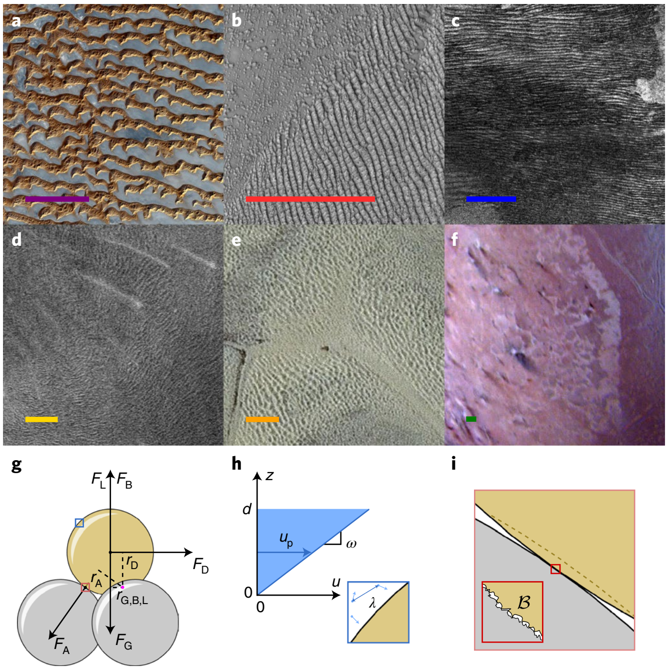

Fig. 1 | Dunes and the forces that create them. a–f, Aeolian features on Earth (**a**), Mars (**b**), Titan (**c**), Venus (**d**), Pluto (**e**) and Triton (**f**). **g**, The forces (F) and moments (r) of lift (L), buoyancy (B), drag (D), gravity (G) and adhesion (A) around the pivot (magenta dot) for the fluid threshold of the yellow particle. **h**, Graphical definitions of fluid velocity (u), elevation (z), vorticity (ω), particle diameter (d) and fluid velocity at the particle centre elevation (u_p), with a close-up of the blue inset in **g** showing the mean free path of gas molecules (λ). **i**, Close-up of the pink inset in **g** of a particle contact and microscopic roughness characterized by $\mathcal{B}$. Credits: **a**, NASA (National Aeronautics and Space Administration)/Goddard Space Flight Center/Ministry of Economy, Trade and Industry of Japan/Earth Remote Sensing Data Analysis Center/Japan Resources Observation System and Space Utilization Organization, and US–Japan Advanced Spaceborne Thermal Emission and Reflection Radiometer Science Team; **b**, NASA/Jet Propulsion Laboratory (JPL)-Caltech/Arizona State University; **c**, NASA/JPL-Caltech/Italian Space Agency; **d**, NASA/JPL; **e**, NASA/Johns Hopkins University Applied Physics Laboratory/Southwest Research Institute; **f**, NASA/JPL. More information on the images in **a–f** is provided in Supplementary Table 2; scale bars are 10 km.

on how rarefied and fast the fluid is[11] (Fig. 2b,e,f). This broad swath in fluid properties is mostly captured by pressure-controlled experiments, with the exception of small bodies that maintain very thin atmospheres such as Triton. There is a distinct lack of experimental data where adhesion dominates the fluid threshold, and where the threshold is extremely high (Fig. 2c,d).

Once wind exceeds the fluid threshold, saltation is initiated. At this point the mechanism for threshold changes qualitatively: the dominant way in which grains leave the bed is by ejection due to impact from colliding grains[1]. The forces used in the fluid threshold above, apart from adhesion, also describe the physics of saltating grain trajectories (Methods). Interestingly, there are two almost universal characteristics of these trajectories: saltators eject from the bed at an approximately fixed angle; and typically only one saltator is ejected per impact, while other grains 'splash' short distances and quickly deposit[17,18]. If we couple trajectory dynamics with a model for the speed ratio between the impacting ($v_\downarrow$) and ejecting ($v_\uparrow$) saltators—that is, the effective restitution coefficient e—we can find the minimum friction velocity necessary to maintain a steady state, $v_\uparrow = e v_\downarrow$ (Fig. 3e). This state corresponds to a balance between the momentum lost during a collision to the granular bed and viscous dissipation, and momentum gained by fluid drag and lift during the hop[19].

The effective restitution coefficient includes contributions from particle elasticity, granular friction and viscous dissipation[10,18,20]. It may be back-calculated from experimental and field studies of the impact threshold, by solving for trajectories at the conditions where the threshold was measured (Supplementary Section 2). We seek an intuitive and parsimonious parameterization for e. Drawing on studies showing that e depends on a competition between particle inertia and viscous dissipation[18,20], we assume that other contributions vary little among materials. To test this idea we examine the relation between e_{10}, the restitution coefficient associated with a fixed common impact angle of −10°, and the Galileo number, $\mathcal{G} = \sqrt{(\rho_s/\rho_f - 1)gd^3}/\nu$ (ρ_s is the solid density, ρ_f is the fluid density and ν is the kinematic viscosity), which has been identified as an important parameter governing sediment transport[6,21] (Fig. 3d and Extended Data Fig. 4). The resulting correlation is strong; we suggest a heuristic logistic functional form for $e_{10}(\mathcal{G})$, where the only free parameter $e_{10}(\mathcal{G} = 10^{\mathcal{C}}) = 1/2$ defines the crossover from the end-member cases of a fully damped and fully elastic impact event (Methods). By fitting to observations we find $\mathcal{C} \approx 1.65$ (Fig. 3c,d), which can be implemented in a forward model to predict the impact threshold. This theory builds on previous contributions[7,19]; the main improvements are that forces are represented more accurately, and that the number of free parameters is reduced because the ejection speed of grains does not need to be prescribed.

The computed impact thresholds cover a span in magnitude that is comparable to the fluid thresholds, with the latter exceeding the former in nearly all cases—probably leading to hysteresis in sediment transport events[5] (Fig. 3a and Supplementary Fig. 2b). Compared with previous theories[5–7] our approach is more accurate when compared with observations, and predicts lower impact thresholds in less dense fluids (Extended Data Figs. 5 and 6). Our formulation of the impact threshold becomes ill defined for small grain sizes (Extended Data Fig. 8 and Methods). This occurs approximately where the two thresholds reach parity, and where turbulent fluctuations—neglected in our Reynolds-averaged description—are expected to become important in determining grain trajectories. While alternative methods avoid this pathology by imposing that the impact threshold smoothly approaches the fluid one in this limit[22], there is a distinct lack of data to test ideas about small grains.

Our theory permits us to resolve characteristic saltator trajectories, and therefore the impact speed (Extended Data Figs. 7 and 9). This characterizes the energy that results in wind-driven sediment attrition, a critical mechanism in wearing down particles and potentially producing dust[23–26]. By employing a canonical model for yield during particle impact[10], using the material properties of sediments (Methods), we inspect the ratio of the impact speed at threshold over the speed required to cause yield, $v_\downarrow^*/v_Y$ (Fig. 3b). This constitutes an attrition parameter; if this ratio is very small, relatively strong sediment particles were probably produced from weathering rather than attrition of bedrock, whereas large values would indicate weak particles that could not survive impact and make dunes. To build intuition regarding the meaning of numerical values for $v_\downarrow^*/v_Y$, we compute them for two representative materials on Earth—quartz and gypsum. While the former is stronger than the latter, both form competent sand grains that round—rather than shatter—when transported by wind[23,25]. Gypsum, however, exhibits substantial attrition over just a few kilometres of transport, while quartz requires an order of magnitude larger distance; their corresponding values for $v_\downarrow^*/v_Y$ differ by roughly 50%. Turning to other planetary bodies, we see striking variability in the attrition susceptibility of candidate dune sands. The slope of the attrition parameter with grain size does not have a consistent sign across environments. More negative slopes may imply efficient production of dust, if there is equal transport susceptibility of grain sizes[27].

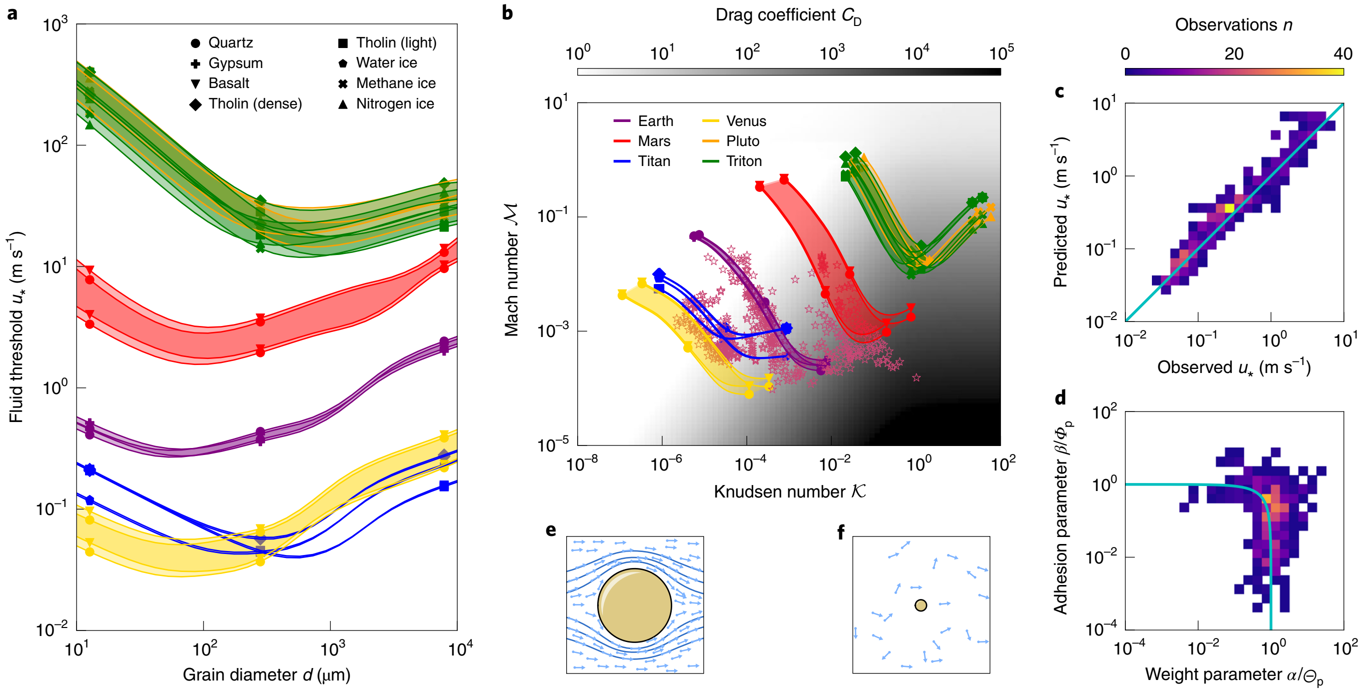

Fig. 2 | Fluid threshold prediction and observations. a, Predicted fluid threshold friction velocities for grains of different candidate and known sediments, on each planetary body (legend for the latter in **b**). **b**, Fluid regime cast in Knudsen ($\mathcal{K}$) and Mach ($\mathcal{M}$) number space for predictions (bands) and observations (stars) at the fluid threshold; the background greyscale gradient indicates C_D. Bands in **a** and **b** show the range based on known temperature and pressure variability. **c**, Histogram comparing observed fluid thresholds and their predicted values; a 1:1 line (cyan) is overlaid. **d**, Equation (1) (cyan) overlaid on a histogram of observations. **e**,**f**, Schematics of the continuum and free-molecular limits corresponding to the $\mathcal{K}$ values above them, respectively.

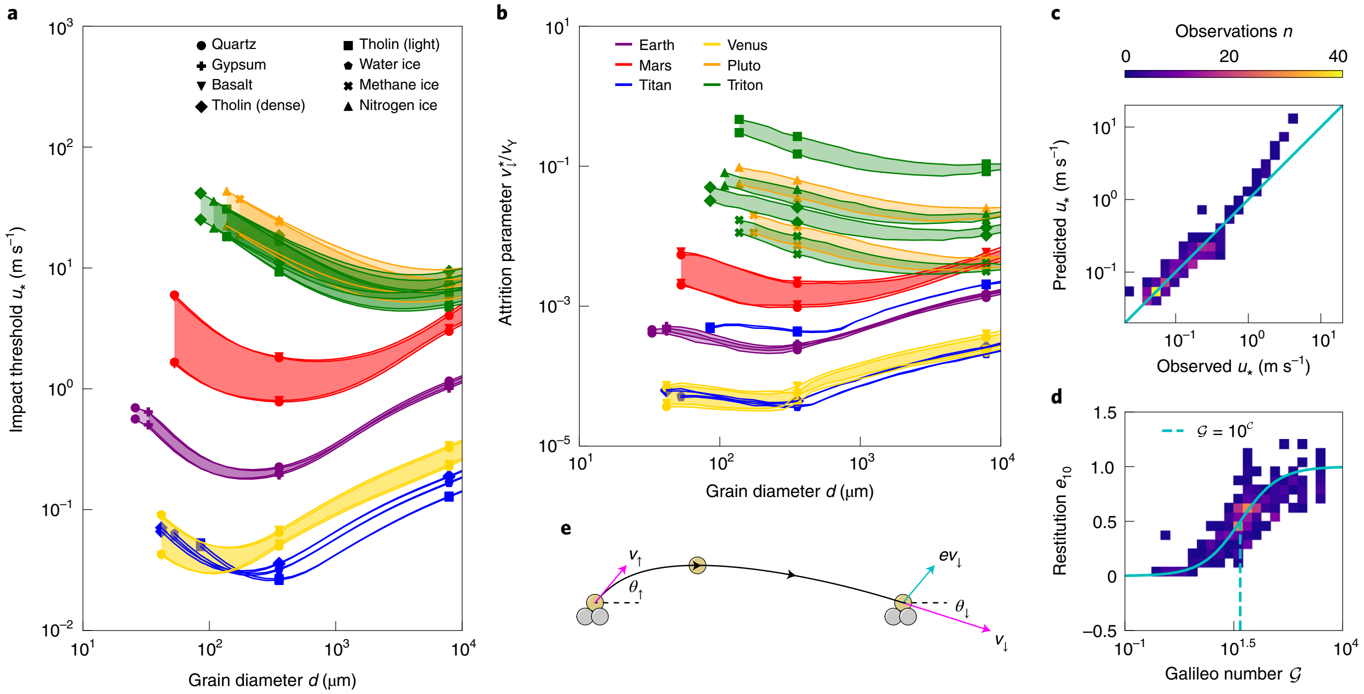

Fig. 3 | Impact threshold prediction and observations. a, Predicted impact threshold friction velocities for grains of different candidate and known sediments on each planetary body. Legends follow those of Fig. 2. **b**, Predicted attrition of characteristic particles at the impact threshold. Bands in **a** and **b** show the ranges for each planet based on known temperature and pressure variability. **c**, Histogram comparing observed impact thresholds and their predicted values; a 1:1 line (cyan) is overlaid. **d**, Heuristic $e_{10}(\mathcal{G})$ (cyan) overlaid on a histogram of observations; the dashed line (cyan) defines the fit parameter $\mathcal{C}$. **e**, Trajectory at the impact threshold for 100 μm basalt on Venus (grains, path and vectors are consistently scaled).

We have highlighted how large variations in atmospheric conditions and particle properties on each planetary body lead to markedly different aeolian sediment transport thresholds by employing better representation of the mechanisms that change substantially outside Earth. Indeed, the minimal effect of environmental and sediment variability on Earth's thresholds is a red herring; these play major roles in all other bodies we study (Fig. 2a). Of course, there are mechanisms known to play a role in the saltation threshold that we have not represented here: notably, capillary[28] and electrostatic forces[29]. Our analysis, however, has revealed that there are potentially important and previously unconsidered mechanisms that we do not currently understand—such as lift at low pressure (Supplementary Section 3) and the fluid threshold in the adhesion limit (Fig. 2d). We do not explicitly account for adhesion effects in the impact threshold theory; some results indicate that adhesion may be neglected for saltation[21].

This work may help to resolve some unsettled debates in planetary aeolian geomorphology. For Pluto, our analysis supports the hypothesis that methane ice constitutes the dunes west of Sputnik Planitia[3], but finds that present-day winds[30] may be insufficient to activate dunes. The dark streaks on Triton are probably inactive after plume deposition, due to high entrainment thresholds and erosion susceptibility[31]. Venusian sands are probably sourced by non-aeolian mechanisms, and transport has negligible hysteresis, akin to water on Earth[7]. On Titan, more work is needed to understand the aggregation and attrition of tholins, but our results support locally sourced and low-density tholin dune sands[4,32]. Finally, on Mars we suggest that ~100-μm-diameter sand grains observed by Curiosity in Gale Crater composing active ripples produce dust through attrition much faster than on Earth[33] (Fig. 3b), and require stronger winds to move than Global Circulation Models predict[14,34]—perhaps through katabatics[35] or strong instability in the boundary layer[36].

Methods

Fluid threshold theory. The schematic in Fig. 1g shows the convention of the force directions and the exact pocket geometry we use. The three-dimensional pocket is created by particles of equal diameter, lying in a horizontal plane in an equilateral triangle. The moments are exact for spheres, and the pivot can be thought of as a line between the contacts of the two bed particles downwind of the threshold particle. The forces, moments and torque balance read

$$\begin{aligned}
F_{\mathrm{A}} &= \tfrac{\pi}{2}\gamma d\, \mathrm{e}^{-\mathcal{B}}, & \tfrac{r_{\mathrm{A}}}{d} &= \tfrac{1}{2\sqrt{2}},\\
F_{\mathrm{D}} &= \tfrac{\pi}{8}C_{\mathrm{D}}\rho_{\mathrm{f}}d^2u_{\mathrm{p}}^2, & \tfrac{r_{\mathrm{D}}}{d} &= \tfrac{1}{\sqrt{6}},\\
F_{\mathrm{L}} &= \tfrac{\pi}{8}C_{\mathrm{L}}\rho_{\mathrm{f}}d^2u_{\mathrm{p}}^2, & \tfrac{r_{\mathrm{L}}}{d} &= \tfrac{1}{4\sqrt{3}}, \; r_{\mathrm{G}}F_{\mathrm{G}} + r_{\mathrm{A}}F_{\mathrm{A}} = \mathcal{A}(r_{\mathrm{D}}F_{\mathrm{D}} + r_{\mathrm{L}}F_{\mathrm{L}}) + r_{\mathrm{B}}F_{\mathrm{B}},\\
F_{\mathrm{B}} &= \tfrac{\pi}{6}g\rho_{\mathrm{f}}d^3, & \tfrac{r_{\mathrm{B}}}{d} &= \tfrac{1}{4\sqrt{3}},\\
F_{\mathrm{G}} &= \tfrac{\pi}{6}g\rho_{\mathrm{s}}d^3, & \tfrac{r_{\mathrm{G}}}{d} &= \tfrac{1}{4\sqrt{3}},
\end{aligned} \tag{2}$$

where $\mathcal{B}$ is the ratio of contact-scale roughness to the interparticle distance in contact[13], C_{L} is the lift coefficient and $\mathcal{A}$ is the ratio of a sphere's frontal area to natural sediment effective frontal area with respect to the flow for drag and lift. Equation (1) is the information above rearranged into a compact and meaningful form, where we have employed accurate ways to model each parameter if need be. Substituting the forces and moments into the torque balance, we can write

$$u_{\mathrm{p}}^2 = \frac{1}{2\sqrt{2}C_{\mathrm{D}} + C_{\mathrm{L}}}\frac{4}{3}\left(\frac{gd(s-1)}{\mathcal{A}} + 3\sqrt{6}\frac{\gamma\,\mathrm{e}^{-\mathcal{B}}}{d\rho_{\mathrm{f}}\mathcal{A}}\right), \tag{3}$$

where s is the ratio $\rho_{\mathrm{s}}/\rho_{\mathrm{f}}$. Now dividing by the left-hand-side and defining α, β, Θ_{p} and Φ_{p} we arrive at equation (1) in the main text:

$$\begin{aligned}
\alpha &= \tfrac{1}{2\sqrt{2}C_{\mathrm{D}}+C_{\mathrm{L}}}\,\tfrac{4}{3\mathcal{A}},\\
\beta &= \tfrac{1}{2\sqrt{2}C_{\mathrm{D}}+C_{\mathrm{L}}}\,\tfrac{4\sqrt{6}\,\mathrm{e}^{-\mathcal{B}}}{\mathcal{A}},\\
\Theta_{\mathrm{p}} &= \tfrac{u_{\mathrm{p}}^2}{gd(s-1)},\\
\Phi_{\mathrm{p}} &= \tfrac{u_{\mathrm{p}}^2 d\rho_{\mathrm{f}}}{\gamma},\\
1 &= \tfrac{\alpha}{\Theta_{\mathrm{p}}} + \tfrac{\beta}{\Phi_{\mathrm{p}}}.
\end{aligned} \tag{4}$$

We have chosen the notation for Θ_{p} because replacing u_{p} with u_* gives the Shields number Θ; Φ_{p} follows suit. All the parameters in α and β are dimensionless, and they encode information about shape and sensitivity. All the parameters in Θ_{p} and Φ_{p} are dimensional, and these encode the system state. If the sum of fractions in equation (1) is greater than unity, the state is below the fluid threshold.

In Fluid threshold fit we find $\mathcal{A}$ and $\mathcal{B}$. In Fluid property theory we find ν (required to link u_{p} with u^* (ref. [37]), as explained in Supplementary Section 4), ρ_f, λ and the speed of sound c; these parameters are required to find C_{D} and C_{L} using the empirical correlations we employ from Loth[11,16]. In Surface energy theory we find γ. Values and ranges for these variables, along with the fixed ones, are given in Supplementary Table 1. Finally, d is the independent parameter. At the fluid threshold of saltation, we assume that the wind profile is at equilibrium with the roughness of the resting grains[37], but does not lose momentum to saltating grains (Supplementary Section 4).

Surface energy theory. The adhesion force between particles depends linearly on γ. Ideally γ is measured, typically in the correct geometry and environment with an atomic force microscope. Without this ability, we employ the Lifshitz theory to estimate the Hamaker constant, A (ref. [13]). For two perfect like spheres, A and γ are coupled such that

$$\gamma = \frac{A}{12\pi d_0^2}, \tag{5}$$

where $d_0 = 0.165$ nm (ref. [13]). Lifshitz theory takes information about the solids in contact and the gas in which they are immersed, and provides an approximation for A such that

$$A = \frac{3}{4}k_{\mathrm{B}}T\left(\frac{\varepsilon_{\mathrm{s}} - \varepsilon_{\mathrm{f}}}{\varepsilon_{\mathrm{s}} + \varepsilon_{\mathrm{f}}}\right)^2 + \frac{3\hbar\nu_{\mathrm{e}}}{16\sqrt{2}}\frac{\left(n_{\mathrm{s}}^2 - n_{\mathrm{f}}^2\right)^2}{\left(n_{\mathrm{s}}^2 + n_{\mathrm{f}}^2\right)^{3/2}}, \tag{6}$$

where subscripts s and f denote solid and fluid, respectively, k_{B} is Boltzmann's constant, T is the temperature, ε is the static relative permittivity, ħ is the reduced Planck constant, ν_{e} is the frequency of the absorption peak (assumed to be $3\times10^{15}\,\mathrm{s}^{-1}$ for all media) and n is the refractive index. n depends on temperature (and pressure for the gas), so over the relatively small variations we consider on each planetary body we assume a linear relationship of n constrained by known values of $n(T, p)$. This calculation is performed for all cases apart from tholin, where γ was measured with an atomic force microscope by Yu et al.[38]. While it is clear that γ depends on the environment from the equation above, in lieu of alternatives we assume to first order that the atomic force microscopy measurement for tholin holds in all cases. In Supplementary Table 3 we provide referenced values for the material-specific constants used in this calculation for all other cases.

Fluid threshold fit. We compiled previously measured fluid threshold friction velocities from experiments and field studies to find the unknown parameter $\mathcal{B}$ (refs. [28,32,39–68]). This parameter is the ratio of the length-scale of surficial particle roughness and the interparticle distance across which adhesion forces act[13], and therefore finding it through regression onto experimental data from natural particles implicitly encodes the role of surficial roughness on natural sediment into the theory, which assumes that the grains are spherical. We chose to only include measurements where the humidity was reported to be less than 15%, to minimize the effect of capillary forces[69]. To implement this fit, all the other parameters that make up equation (1) must be known for each observation. We used the variables stated in each paper where possible. Otherwise, we assumed that measurements were taken at $T = 20$ °C and standard pressure for the elevation at which they were measured, then made use of the equations in Fluid property theory if required. Not all papers report γ for their experiments; in lieu of this important parameter, we used reference Hamaker constants from measurements in other literature for each sediment material[13,38,70,71] (or a similar material if a measurement could not be found: that is, clover seed was assumed to adhere the same as walnut shells). These data are collated in Supplementary Data 1.

In the main text and result we only fit using one parameter, $\mathcal{B}$; there is however an additional free parameter, $\mathcal{A}$, that in principle should depend on the sediment shape[6]. In an ideal configuration $\mathcal{A} = 1$, and when allowing it to vary freely alongside $\mathcal{B}$ to match observations we find it to be $\mathcal{A} = 1.01$. Given the similarity between these results, and the negligible effect on accuracy between them (Extended Data Fig. 2a,b), we fix $\mathcal{A} = 1$. The fitting parameters are found by minimizing

$$\sum_{n=1}^{N}\left(\frac{u_{*,\mathrm{observed}}}{u_{*,\mathrm{predicted}}} - 1\right)^2, \tag{7}$$

with $N = 567$ being the number of fluid threshold measurements compiled in this study. This form of the loss function was used to ensure that there is no bias toward the magnitude of u_*.

Fluid property theory. We assume that the gases can be described as ideal, with the kinetic theory of gases, and with respect to viscosity using a Lennard-Jones pair potential between molecules. This allows us to find the fluid properties related to sediment transport using just temperature, pressure and material constants. The dynamic viscosity ($\mu = \rho_f \nu$) is found using the Lennard-Jones model[12],

$$T_* = \frac{Tk_B}{\varepsilon_T}, \tag{8}$$

$$\Omega_*^{(2,2)} = A_T T_*^{-B_T} + C_T \, e^{-D_T T_*} + E_T \, e^{-G_T T_*}, \tag{9}$$

$$\mu = 2.6693 \times 10^{-6} \frac{\sqrt{MT}}{\sigma^2 \Omega_*^{(2,2)}}, \tag{10}$$

where $A_T = 1.16145$, $B_T = 0.14874$, $C_T = 0.52487$, $D_T = 0.77320$, $E_T = 2.16178$ and $G_T = 2.43787$ are fit parameters for the reduced viscosity collision integral $\Omega_*^{(2,2)}$ (ref. [72]). The Boltzmann constant is 1.38×10^{-23} J K^{-1}. Material constants σ, ε_T and M are given in Supplementary Table 3. This formulation is used, instead of the Sutherland formula employed in other sediment transport studies[3,5], because it extrapolates more reliably, since it does not assume hard-sphere repulsion at short range.

Fluid density is found using the ideal gas law[12],

$$\rho_f = \frac{pM}{RT}, \tag{11}$$

where $R = 8.314$ J K^{-1} mol^{-1} is the gas constant.

The mean free path is found using the kinetic theory of gases[12],

$$\lambda = \frac{\mu}{p}\sqrt{\frac{\pi RT}{2M}}. \tag{12}$$

The Mach ($\mathcal{M} = c/u_p$), Knudsen ($\mathcal{K} = \lambda/d$) and Reynolds ($\mathcal{R} = u_p d/\nu$) numbers are related by

$$\mathcal{K} = \frac{\mathcal{M}}{\mathcal{R}}\sqrt{\frac{\pi\gamma_C}{2}}, \tag{13}$$

where γ_C is the heat capacity ratio, a material constant given in Supplementary Table 1. This is useful when interpreting Fig. 2b, as the drag coefficient (and 'crisis') is typically displayed as a function of $\mathcal{R}$.

Grain trajectory theory. Grains in flight obey an equation of motion defined by the force balance,

$$m_p \frac{\partial v}{\partial t} = F_D + F_L + F_G + F_B, \tag{14}$$

where m_p is the particle mass, v is the particle velocity and t is time. Substituting the forces in Fluid threshold theory and rearranging, we find the following equation of motion (written in the complex plane for simplicity):

$$\frac{\partial v}{\partial t} = \frac{3}{4}(C_D + iC_L)\frac{|u_p(z_p) - v|(u_p(z_p) - v)}{sd} - i\left(1 - \frac{1}{s}\right)g, \tag{15}$$

where $v = v_x + iv_z$ is the particle velocity vector, $u_p = u_x(z_p) + 0i$ is the horizontal fluid speed at the particle centre, z_p is the elevation (where zero is defined at the base of a particle at rest on the bed) and g is the acceleration due to gravity. This equation states that particles have drag, lift and effective weight altering their path as they are in flight. The drag and lift magnitudes depend on the square of the relative speed of the particle with respect to the flow, as to their angles, while gravity acts constantly and always downward. Implicit in this formulation is that the particles do not extract momentum from the flow, since the formulation of u_x we employ is only affected by the roughness that grains impart to the flow[37]. This is a common and reasonable assumption at the impact threshold[5–7], since this is the edge of the regime where there are no particles moving. Solving this equation for a grain trajectory, from ejection to impact, is an initial-value problem that requires numerical integration. Position, velocity and acceleration are all present in this ordinary differential equation. We define the initial and final values of the velocity vectors as

$$\begin{aligned} v|_{(z_p=d/2)\wedge(t=0)} &= v_\uparrow \, e^{i\theta_\uparrow}, \\ v|_{(z_p=d/2)\wedge(t\neq0)} &= v_\downarrow \, e^{i\theta_\downarrow}, \end{aligned} \tag{16}$$

respectively, where $\theta_\uparrow = 50°$ is the fixed ejection angle[17,18] and $\theta_\downarrow$ is the impact angle. For a steady-state trajectory, the relation $v_\uparrow = ev_\downarrow$ holds, where e is the ratio of momentum maintained in saltation. In Restitution parameterization we show how e is parameterized using $\theta_\downarrow$ and $\mathcal{G}$. Since we seek a solution to an ordinary differential equation where the target initial value must be chosen as a function of the final value, we must not only numerically integrate the initial-value problem, but also iteratively converge on the steady-state solution. Please see the code availability statement for our approach to this problem implemented using SciPy[73].

In Extended Data Figure 7 it is clear that there are multiple pairs of u_* and $v_\uparrow$ such that $v_\uparrow = ev_\downarrow$; however, we seek a unique pair that defines the impact threshold. We require the minimum friction velocity for which this equality holds. Inspecting a well posed case (Extended Data Figs. 7 and 8a), for each curve of fixed friction velocity, all ejection speeds apart from the solution result in the ratio of the ejection to impact speeds being too large—that is, the particles do not gain enough momentum during flight to sustain transport. Coupling these two critical ideas, we define the impact threshold friction velocity as the one that produces a trajectory such that the ratio of ejection to impact speed (normalized by impact angle, see Restitution parameterization) is equal to the restitution coefficient corresponding to the system's Galileo number. Solving for this case requires a third layer of numerical methods that is implemented in our public code.

Restitution parameterization. To find a restitution coefficient parameterization, we compiled previously measured impact threshold friction velocities from experiments and field studies[41–43,59,64,74–80]. As noted in the main text, this choice of parameterization requires a single fit parameter, $\mathcal{C}$. To find $\mathcal{C}$, all the other parameters that make up the trajectory equation of motion (Grain trajectory theory) must be known for each observation. As for the fluid threshold measurements, we used the variables stated in the paper where possible. Otherwise, we assumed that measurements were taken at $T = 20$ °C and standard pressure for the elevation at which they were measured, then made use of the equations in Fluid property theory if required. These data are collated in Supplementary Data 2. With these known, we calculate $v_\uparrow/v_\downarrow$ and $\theta_\downarrow$ for each measurement using the observed u_*; our theory for e should ideally be equal to $v_\uparrow/v_\downarrow$ for each measurement.

We also compiled data from other studies where the restitution coefficient of particles hitting a loose bed was explicitly measured[17,18,81–86]. If these measurements were from studies where wind was blowing particles, we only considered the measurements at the impact threshold. This distinction is important since the bulk restitution will be altered by particles extracting momentum from the flow and bed particles not being at rest. As above, we used the variables stated in the paper where possible. Otherwise, we assumed that measurements were taken at $T = 20$ °C and standard pressure for the elevation at which they were measured, then made use of the equations in Fluid property theory if required. These data are collated in Supplementary Data 3. It is clear from one of these studies[18] that a good approximation for the effect of impact angle on restitution—also employed elsewhere—is[87]

$$\frac{e}{e_{10}} = \frac{1 - e_\alpha \sin(\theta_\downarrow)}{1 - e_\alpha \sin(10)}, \tag{17}$$

where $e_\alpha \approx 0.828$ is found experimentally[18]. We choose 10° arbitrarily, but require that all restitution coefficients are normalized as if they are found from equal impact angles when trying to derive a parameterization.

Relevant studies indicate that the restitution coefficient of saltators is independent of impact speed[17,18,81,85,86,88,89]. This contrasts with the restitution coefficient of a single particle impacting a plane, which increases with impact speed after a threshold and is predictive using the Stokes number[90,91]. For the narrowly defined restitution coefficient we attempt to accurately model, we are interested in non-unique saltators in the limit of vanishing sediment flux during events where a loose bed also produces splash. In this case, we seek a non-dimensional parameter that does not include a velocity scale, and clearly relates to the restitution coefficient from experiments. Guided by the trend for both explicit and implicit data (Extended Data Fig. 4c), we suggest to first order that

$$e_{10} = \frac{\mathcal{G}}{10^{\mathcal{C}} + \mathcal{G}}. \tag{18}$$

$\mathcal{C}$ is the distillation of multiple mechanisms that produce bulk restitution of the saltating particle, and includes the role of shape variability in natural sediment grains[91] through regression onto the experiments where they are employed. We find $\mathcal{C} \approx 1.65$ using a least-square regression onto the data described above. This approach assumes imperfectly that the restitution coefficient could potentially reach unreasonably high values (such that saltation would sustain without fluid flow, that is $e > 1$) if both $\mathcal{G}$ and $\theta_\downarrow$ are large. In lieu of a more appropriate data-informed alternative, however, we use the accurate formulation above, noting that our predictions lie well outside these unreasonable regimes. This formulation is consistent with intuition (as described in the main text) and data where available[85] (Extended Data Fig. 4).

Yield speed theory. We assume that the yield speed (v_Y) for two like spheres is modelled by[10]

$$v_Y = \sqrt{\frac{26Y^5}{E_*^4 \rho_s}}, \tag{19}$$

where Y is the yield stress, $E_* = E/2(1 - V^2)$ is the effective elastic modulus (E) and V is the Poisson ratio (upper case here to avoid confusion with the particle speed used elsewhere in this manuscript). This formulation is based on the Von Mises criterion that solids yield when the maximum pressure exerted at the contact exceeds $1.6Y$. The yield stress is not necessarily related to the elastic modulus in the same way for all materials; in lieu of yield stress data for all materials used in this study, however, for geologically relevant materials the following three semiempirical relationships are relatively accurate:

$$\begin{aligned}\tfrac{H}{Y} &= 0.19 + 1.6\log_{10}\left(\tfrac{E}{Y}\tan(\beta_{\mathrm{I}})\right),\\ H &= 2\times10^{-5}E^{4/3},\\ \tfrac{E}{E_0} &= \tfrac{2T_{\mathrm{m}}-T}{2T_{\mathrm{m}}-T_0},\end{aligned}\qquad(20)$$

from ref. [92], ref. [4] and ref. [93], respectively, where H is the hardness measured with a nanoindenter of angle β_{I}, $E_0(T_0)$ is the elastic modulus measured at temperature T_0 and T_{m} is the melting temperature. We note that it would be ideal to use a theory on chipping of geologic materials over this approach, but current theories require measurements of fracture toughness that have not been taken for material and environments applicable to this study[24,94]. In the special case of 'tholin (light)', we crudely assume that the yield stress (Y_{TL}) is related to the yield stress of 'tholin (dense)' (Y_{TD}) by the ratio of their densities, such that $Y_{\mathrm{TL}}/Y_{\mathrm{TD}}=\rho_{\mathrm{TL}}/\rho_{\mathrm{TD}}$, since the yield stress should decrease with aggregate density and experimental evidence is not available. We treat this yield speed as a characteristic value of attrition, instead of a robust predictor.

Data availability

All data are available in the Supplementary Data files. Source data are provided with this paper.

Code availability

The code used to produce this paper can be accessed at https://doi.org/10.5281/zenodo.6480898.

Received: 2 December 2020; Accepted: 30 March 2022;

References

1. Bagnold, R. A. *The Physics of Blown Sand and Desert Dunes* (Courier, 1941).
2. Hayes, A. G. Dunes across the Solar System. *Science* **360**, 960–961 (2018).
3. Telfer, M. W. et al. Dunes on Pluto. *Science* **360**, 992–997 (2018).
4. Yu, X., Hörst, S. M., He, C., McGuiggan, P. & Crawford, B. Where does Titan sand come from: insight from mechanical properties of Titan sand candidates. *J. Geophys. Res. Planets* **123**, 2310–2321 (2018).
5. Kok, J. F. An improved parameterization of wind-blown sand flux on Mars that includes the effect of hysteresis. *Geophys. Res. Lett.* **37**, L12202 (2010).
6. Pähtz, T. & Durán, O. The cessation threshold of nonsuspended sediment transport across aeolian and fluvial environments. *J. Geophys. Res. Earth Surf.* **123**, 1638–1666 (2018).
7. Claudin, P. & Andreotti, B. A scaling law for aeolian dunes on Mars, Venus, Earth, and for subaqueous ripples. *Earth Planet. Sci. Lett.* **252**, 30–44 (2006).
8. Shao, Y. & Lu, H. A simple expression for wind erosion threshold friction velocity. *J. Geophys. Res. Atmos.* **105**, 22437–22443 (2000).
9. Iversen, J. D. & White, B. R. Saltation threshold on Earth, Mars and Venus. *Sedimentology* **29**, 111–119 (1982).
10. Johnson, K. L. *Contact Mechanics* (Cambridge Univ. Press, 1987).
11. Loth, E. Compressibility and rarefaction effects on drag of a spherical particle. *AIAA J.* **46**, 2219–2228 (2008).
12. Byron Bird, R. Transport phenomena. *Appl. Mech. Rev.* **55**, R1–R4 (2002).
13. Israelachvili, J. N. *Intermolecular and Surface Forces* (Academic, 2011).
14. Ayoub, F. et al. Threshold for sand mobility on Mars calibrated from seasonal variations of sand flux. *Nat. Commun.* **5**, 5096 (2014).
15. Wiberg, P. L. & Smith, J. D. Calculations of the critical shear stress for motion of uniform and heterogeneous sediments. *Water Resour. Res.* **23**, 1471–1480 (1987).
16. Loth, E. Lift of a spherical particle subject to vorticity and/or spin. *AIAA J.* **46**, 801–809 (2008).
17. Anderson, R. S. & Haff, P. K. Simulation of eolian saltation. *Science* **241**, 820–823 (1988).
18. Beladjine, D., Ammi, M., Oger, L. & Valance, A. Collision process between an incident bead and a three-dimensional granular packing. *Phys. Rev. E* **75**, 061305 (2007).
19. Andreotti, B. A two-species model of aeolian sand transport. *J. Fluid Mech.* **510**, 47–70 (2004).
20. Gondret, P., Lance, M. & Petit, L. Bouncing motion of spherical particles in fluids. *Phys. Fluids* **14**, 643–652 (2002).
21. Pähtz, T. & Durán, O. Unification of aeolian and fluvial sediment transport rate from granular physics. *Phys. Rev. Lett.* **124**, 168001 (2020).
22. Durán, O., Claudin, P. & Andreotti, B. On aeolian transport: grain-scale interactions, dynamical mechanisms and scaling laws. *Aeolian Res.* **3**, 243–270 (2011).
23. Jerolmack, D. J., Reitz, M. D. & Martin, R. L. Sorting out abrasion in a gypsum dune field. *J. Geophys. Res. Earth Surf.* **116**, F02003 (2011).
24. Ghadiri, M. & Zhang, Z. Impact attrition of particulate solids. Part 1: A theoretical model of chipping. *Chem. Eng. Sci.* **57**, 3659–3669 (2002).
25. Crouvi, O., Amit, R., Enzel, Y., Porat, N. & Sandler, A. Sand dunes as a major proximal dust source for late Pleistocene loess in the Negev Desert, Israel. *Quat. Res.* **70**, 275–282 (2008).
26. Swet, N., Kok, J., Huang, Y., Yizhaq, H. & Katra, I. Low dust generation potential from active sand grains by wind abrasion. *J. Geophys. Res. Earth Surf.* **125**, e2020JF005545 (2020).
27. Martin, R. L. & Kok, J. F. Size-independent susceptibility to transport in aeolian saltation. *J. Geophys. Res. Earth Surf.* **124**, 1658–1674 (2019).
28. McKenna Neuman, C. & Sanderson, S. Humidity control of particle emissions in aeolian systems. *J. Geophys. Res. Earth Surf.* **113**, F02S14 (2008).
29. Kok, J. F. & Renno, N. O. Electrostatics in wind-blown sand. *Phys. Rev. Lett.* **100**, 014501 (2008).
30. Gladstone, G. R. & Young, L. A. New Horizons observations of the atmosphere of Pluto. *Annu. Rev. Earth Planet. Sci.* **47**, 119–140 (2019).
31. Sagan, C. & Chyba, C. Triton's streaks as windblown dust. *Nature* **346**, 546–548 (1990).
32. Burr, D. M. et al. Higher-than-predicted saltation threshold wind speeds on Titan. *Nature* **517**, 60–63 (2015).
33. Weitz, C. M. et al. Sand grain sizes and shapes in eolian bedforms at Gale Crater, Mars. *Geophys. Res. Lett.* **45**, 9471–9479 (2018).
34. Banfield, D. et al. The atmosphere of Mars as observed by InSight. *Nat. Geosci.* **13**, 190–198 (2020).
35. Ewing, R. C., Peyret, A.-P. B., Kocurek, G. & Bourke, M. Dune field pattern formation and recent transporting winds in the Olympia Undae Dune Field, north polar region of Mars. *J. Geophys. Res. Planets* **115**, E08005 (2010).
36. Gunn, A. et al. Circadian rhythm of dune-field activity. *Geophys. Res. Lett.* **48**, e2020GL090924 (2021).
37. Guo, J. & Julien, P. Y. *Buffer Law and Transitional Roughness Effect in Turbulent Open-Channel Flows* Civil Engineering Faculty Publications 5 (Univ. of Nebraska—Lincoln, 2007).
38. Yu, X., Hörst, S. M., He, C., McGuiggan, P. & Bridges, N. T. Direct measurement of interparticle forces of titan aerosol analogs ('tholin') using atomic force microscopy. *J. Geophys. Res. Planets* **122**, 2610–2622 (2017).
39. Swann, C., Sherman, D. & Ewing, R. Experimentally-derived thresholds for windblown sand on Mars. *Geophys. Res. Lett.* **47**, e2019GL084484 (2019).
40. Baas, A. C. & Sherman, D. J. Spatiotemporal variability of aeolian sand transport in a coastal dune environment. *J. Coast. Res.* **22**, 1198–1205 (2006).
41. Bagnold, R. A. The size-grading of sand by wind. *Proc. R. Soc. A* **163**, 250–264 (1937).
42. Burr, D. M. et al. A wind tunnel study of the effect of intermediate density ratio on saltation threshold. *Aeolian Res.* **45**, 100601 (2020).
43. Chepil, W. Dynamics of wind erosion: II. Initiation of soil movement. *Soil Sci.* **60**, 397 (1945).
44. Chepil, W. Properties of soil which influence wind erosion: IV. State of dry aggregate structure. *Soil Sci.* **72**, 387–402 (1951).
45. Del Bello, E. et al. Experimental simulations of volcanic ash resuspension by wind under the effects of atmospheric humidity. *Sci. Rep.* **8**, 14509 (2018).
46. Dong, Z., Liu, X., Wang, H. & Wang, X. Aeolian sand transport: a wind tunnel model. *Sediment. Geol.* **161**, 71–83 (2003).
47. Fletcher, B. The incipient motion of granular materials. *J. Phys. D* **9**, 2471 (1976).
48. Greeley, R., Iversen, J., Pollack, J., Udovich, N. & White, B. Wind tunnel studies of Martian aeolian processes. *Proc. R. Soc. A* **341**, 331–360 (1974).
49. Greeley, R., White, B., Leach, R., Iversen, J. & Pollack, J. Mars: wind friction speeds for particle movement. *Geophys. Res. Lett.* **3**, 417–420 (1976).
50. Greeley, R., Leach, R., White, B., Iversen, J. & Pollack, J. Threshold windspeeds for sand on Mars: wind tunnel simulations. *Geophys. Res. Lett.* **7**, 121–124 (1980).
51. Greeley, R. et al. Windblown sand on Venus: preliminary results of laboratory simulations. *Icarus* **57**, 112–124 (1984).
52. Hong, C., Xueyong, Z., Chenchen, L., Jiajia, H. & Yongqiu, W. Transport mass of creeping sand grains and their movement velocities. *J. Geophys. Res. Atmos.* **118**, 6374–6382 (2013).
53. Horikawa, K. & Shen, H. W. *Sand Movement by Wind Action: on the Characteristics of Sand Traps* Technical Memorandum 119 (US Beach Erosion Board, 1960).
54. Iversen, J. D. & Rasmussen, K. R. The effect of surface slope on saltation threshold. *Sedimentology* **41**, 721–728 (1994).
55. Iversen, J., Pollack, J. B., Greeley, R. & White, B. R. Saltation threshold on Mars: the effect of interparticle force, surface roughness, and low atmospheric density. *Icarus* **29**, 381–393 (1976).

56. Kadib, A. *A Function for Sand Movement by Wind* Technical Report (Univ. of California, Berkeley, Institute of Engineering Research, 1965).
57. Li, B. & McKenna Neuman, C. Boundary-layer turbulence characteristics during aeolian saltation. *Geophys. Res. Lett.* **39**, L11402 (2012).
58. Marshall, J. R. & Greeley, R. An experimental study of aeolian structures on Venus. *J. Geophys. Res.: Planets* **97**, 1007–1016 (1992).
59. Martin, R. L. & Kok, J. F. Wind-invariant saltation heights imply linear scaling of aeolian saltation flux with shear stress. *Sci. Adv.* **3**, e1602569 (2017).
60. McKenna-Neuman, C. & Nickling, W. A theoretical and wind tunnel investigation of the effect of capillary water on the entrainment of sediment by wind. *Can. J. Soil Sci.* **69**, 79–96 (1989).
61. Merrison, J., Jensen, J., Kinch, K., Mugford, R. & Nørnberg, P. The electrical properties of Mars analogue dust. *Planet. Space Sci.* **52**, 279–290 (2004).
62. Nalpanis, P., Hunt, J. & Barrett, C. Saltating particles over flat beds. *J. Fluid Mech.* **251**, 661–685 (1993).
63. Nickling, W. The stabilizing role of bonding agents on the entrainment of sediment by wind. *Sedimentology* **31**, 111–117 (1984).
64. Selah, A. & Fryrear, D. Threshold wind velocities of wet soils as affected by wind blown sand. *Soil Sci.* **160**, 304–309 (1995).
65. Shao, Y. & Mikami, M. Heterogeneous saltation: theory, observation and comparison. *Bound.-Layer Meteorol.* **115**, 359–379 (2005).
66. Svasek, J. & Terwindt, J. Measurements of sand transport by wind on a natural beach. *Sedimentology* **21**, 311–322 (1974).
67. Williams, J. J., Butterfield, G. R. & Clark, D. G. Aerodynamic entrainment threshold: effects of boundary layer flow conditions. *Sedimentology* **41**, 309–328 (1994).
68. Williams, J. J. *Aeolian Entrainment Thresholds in a Developing Boundary Layer*. PhD thesis, Queen Mary Univ. of London (1986).
69. Seiphoori, A., Ma, X.-g., Arratia, P. E. & Jerolmack, D. J. Formation of stable aggregates by fluid-assembled solid bridges. *Proc. Natl Acad. Sci. USA* **117**, 3375–3381 (2020).
70. Bergström, L. Hamaker constants of inorganic materials. *Adv. Colloid Interface Sci.* **70**, 125–169 (1997).
71. Médout-Marère, V. A simple experimental way of measuring the Hamaker constant a_{11} of divided solids by immersion calorimetry in apolar liquids. *J. Colloid Interface Sci.* **228**, 434–437 (2000).
72. Neufeld, P. D., Janzen, A. & Aziz, R. Empirical equations to calculate 16 of the transport collision integrals $\omega^{(l,s)*}$ for the Lennard-Jones (12–6) potential. *J. Chem. Phys.* **57**, 1100–1102 (1972).
73. Virtanen, P. et al. SciPy 1.0: fundamental algorithms for scientific computing in Python. *Nat. Methods* **17**, 261–272 (2020).
74. Andreotti, B., Claudin, P. & Pouliquen, O. Measurements of the aeolian sand transport saturation length. *Geomorphology* **123**, 343–348 (2010).
75. Andreotti, B., Claudin, P., Iversen, J. J., Merrison, J. P. & Rasmussen, K. R. A lower-than-expected saltation threshold at Martian pressure and below. *Proc. Natl Acad. Sci. USA* **118**, e2012386118 (2021).
76. Cornelis, W. M., Gabriels, D. & Hartmann, R. A parameterisation for the threshold shear velocity to initiate deflation of dry and wet sediment. *Geomorphology* **59**, 43–51 (2004).
77. Iversen, J. D. & Rasmussen, K. R. The effect of wind speed and bed slope on sand transport. *Sedimentology* **46**, 723–731 (1999).
78. Jones, J. & Willetts, B. Errors in measuring uniform aeolian sand flow by means of an adjustable trap. *Sedimentology* **26**, 463–468 (1979).
79. Li, B., Ellis, J. T. & Sherman, D. J. Estimating the impact threshold for wind-blown sand. *J. Coast. Res.* **70**, 627–632 (2014).
80. Zingg, A. Wind tunnel studies of the movement of sedimentary material. In *Proc. 5th Hydraulic Conference Bulletin* Vol. 34, 111–135 (Institute of Hydraulics Iowa City, 1953).
81. Anderson, R. S. & Haff, P. K. Wind modification and bed response during saltation of sand in air. In *Aeolian Grain Transport 1* (eds Barndorff-Nielsen, O.E. & Willetts, B.B.) 21–51 (Springer, 1991).
82. Charru, F., Mouilleron, H. & Eiff, O. Erosion and deposition of particles on a bed sheared by a viscous flow. *J. Fluid Mech.* **519**, 55–80 (2004).
83. Ferdowsi, B., Ortiz, C. P., Houssais, M. & Jerolmack, D. J. River-bed armouring as a granular segregation phenomenon. *Nat. Commun.* **8**, 1363 (2017).
84. Nishimura, K. & Hunt, J. Saltation and incipient suspension above a flat particle bed below a turbulent boundary layer. *J. Fluid Mech.* **417**, 77–102 (2000).
85. Rice, M. A., Willetts, B. B. & McEwan, I. An experimental study of multiple grain-size ejecta produced by collisions of saltating grains with a flat bed. *Sedimentology* **42**, 695–706 (1995).
86. Rioual, F., Valance, A. & Bideau, D. Experimental study of the collision process of a grain on a two-dimensional granular bed. *Phys. Rev. E* **62**, 2450 (2000).
87. Creyssels, M. et al. Saltating particles in a turbulent boundary layer: experiment and theory. *J. Fluid Mech.* **625**, 47–74 (2009).
88. Werner, B. T. *A Physical Model of Wind-Blown Sand Transport*. PhD thesis, California Institute of Technology (1987).
89. Werner, B. & Haff, P. The impact process in aeolian saltation: two-dimensional simulations. *Sedimentology* **35**, 189–196 (1988).
90. Gondret, P., Hallouin, E., Lance, M. & Petit, L. Experiments on the motion of a solid sphere toward a wall: from viscous dissipation to elastohydrodynamic bouncing. *Phys. Fluids* **11**, 2803–2805 (1999).
91. Schmeeckle, M. W., Nelson, J. M., Pitlick, J. & Bennett, J. P. Interparticle collision of natural sediment grains in water. *Water Resour. Res.* **37**, 2377–2391 (2001).
92. Evans, B. & Goetze, C. The temperature variation of hardness of olivine and its implication for polycrystalline yield stress. *J. Geophys. Res. Solid Earth* **84**, 5505–5524 (1979).
93. Courtney, T. H. *Mechanical Behavior of Materials* (Waveland, 2005).
94. Domokos, G., Jerolmack, D. J., Kun, F. & Török, J. Plato's cube and the natural geometry of fragmentation. *Proc. Natl Acad. Sci. USA* **117**, 18178–18185 (2020).

Acknowledgements

We thank P. Claudin, B. Andreotti, C. Thom, A. Seiphoori and B. Ferdowsi for insightful discussions. D.J.J. acknowledges support from the Army Research Office, grant 569074. Acknowledgement is made to the Donors of the American Chemical Society Petroleum Research Fund for partial support of this research through grant 61536-ND8 to D.J.J.

Author contributions

Conceptualization, data curation, formal analysis, investigation, software, validation, visualization, writing—original draft, A.G.; methodology, project administration, writing—review & editing, A.G. and D.J.J.; resources, funding acquisition, supervision, D.J.J.

Competing interests

The authors declare no competing interests.

Additional information

Extended data is available for this paper at https://doi.org/10.1038/s41550-022-01669-0.

Supplementary information The online version contains supplementary material available at https://doi.org/10.1038/s41550-022-01669-0.

Correspondence and requests for materials should be addressed to Douglas J. Jerolmack.

Peer review information *Nature Astronomy* thanks Ping Wang and Hezi Yizhaq for their contribution to the peer review of this work.

Reprints and permissions information is available at www.nature.com/reprints.

Publisher's note Springer Nature remains neutral with regard to jurisdictional claims in published maps and institutional affiliations.

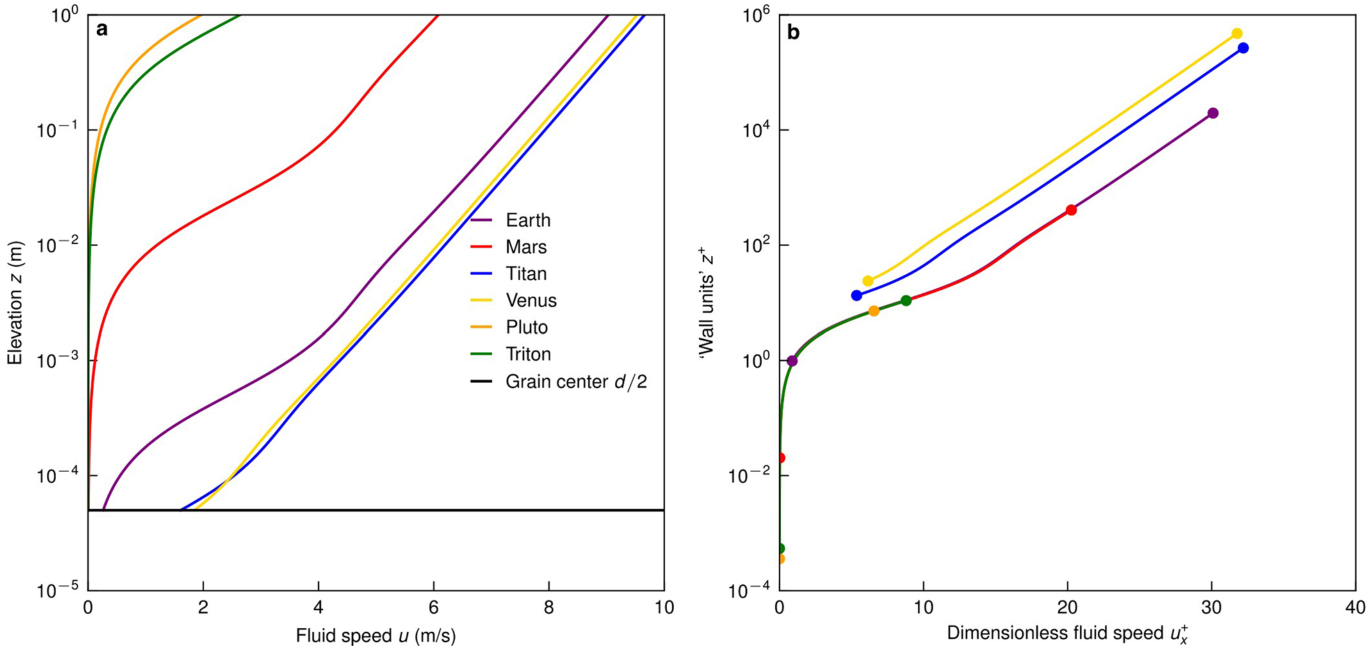

Extended Data Fig. 1 | Wind profiles. (a) Mean horizontal wind speed with elevation for a fixed friction velocity ($u_* = 0.3$ m/s) and grain size ($d = 100\mu$m) for the six bodies of interest using the empirical relation in Supplementary Information Text S4. The grain center is denoted with a black line.
(b) Dimensionless presentation of (a), where $u_x^+ = u/u_*$ and $z^+ = zu_*/\upsilon$.

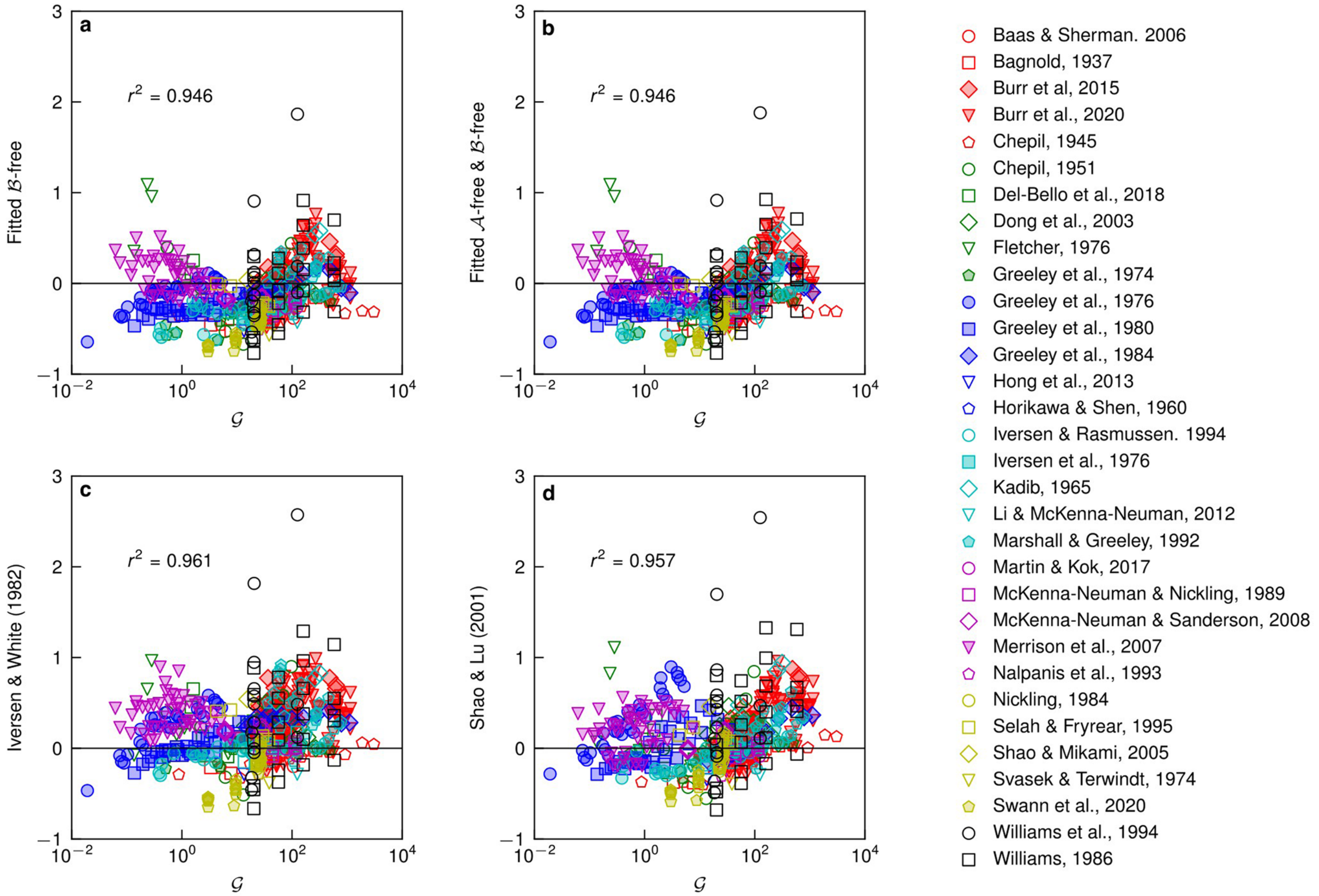

Extended Data Fig. 2 | Fluid threshold prediction comparison to data. Four methods for predicting the fluid threshold are compared to observed data, where the vertical axis is $u_{*,observed}/u_{*,predicted} - 1$ (for the labelled prediction) and the horizontal axis is the Galileo number, $\mathcal{G}$. References for the observations are given on the right, where markers with shaded interiors signify experiments not using standard Earth conditions. The correlation coefficient (r^2) for each log-log comparison of $u_{*,observed}$ versus is $u_{*,predicted}$ (that is Fig. 2c) is annotated. **(a)** The prediction in the main text, where A=1. **(b)** The prediction except $\mathcal{A}$ is a free-parameter. **(c)** The prediction using the empirical relation of Iversen & White (1982). **(d)** The prediction using the semiempirical theory of Shao & Lu (2000).

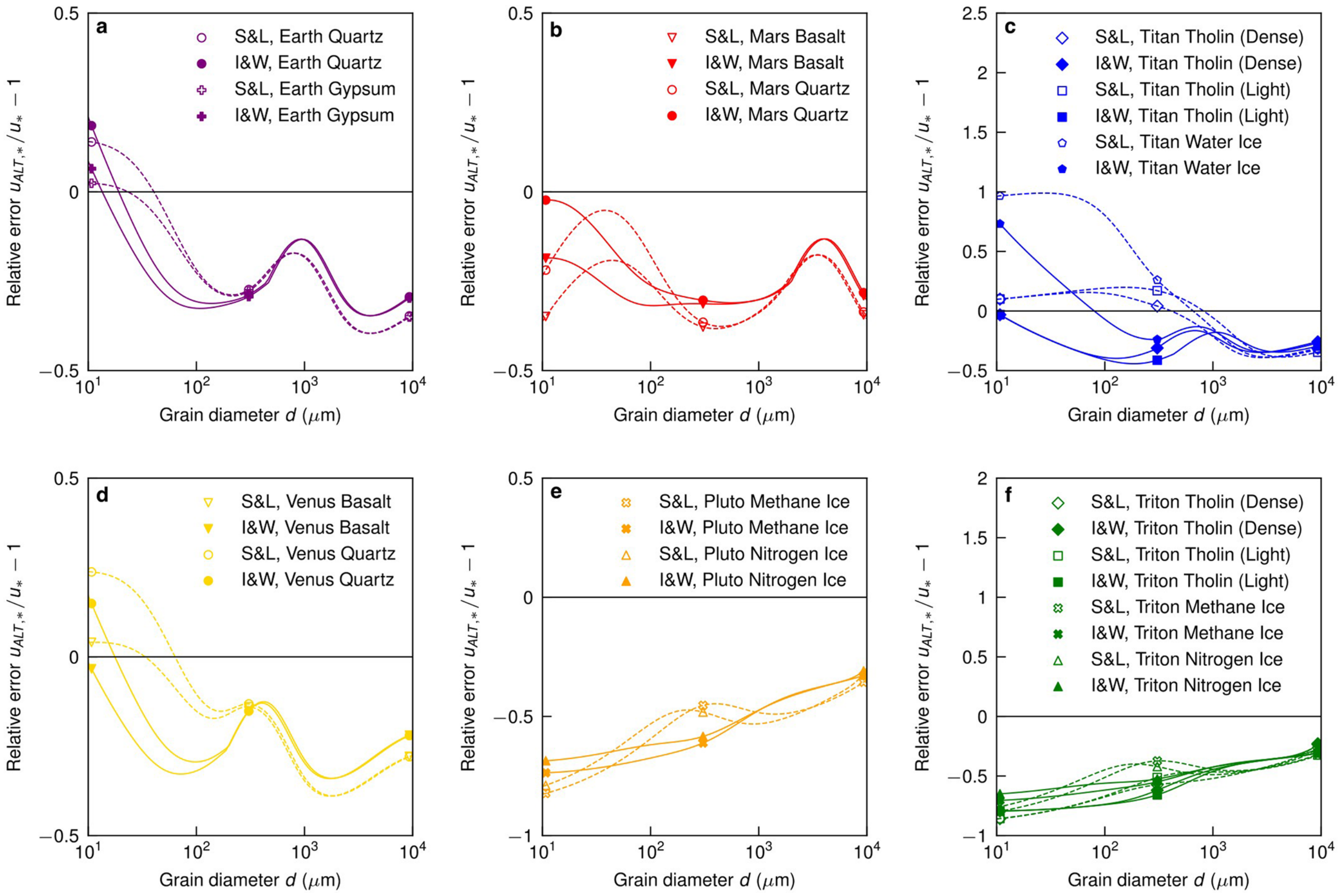

Extended Data Fig. 3 | Fluid threshold prediction comparison to each other. The relative error between the alternative predictions of Shao & Lu (2000) (S&L) and Iversen & White (1982) (I&W) with the prediction in the main text for the fluid threshold for average conditions on each body. Each sediment candidate is given for **(a)** Earth, **(b)** Mars, **(c)** Titan, **(d)** Venus, **(e)** Pluto and **(f)** Triton.

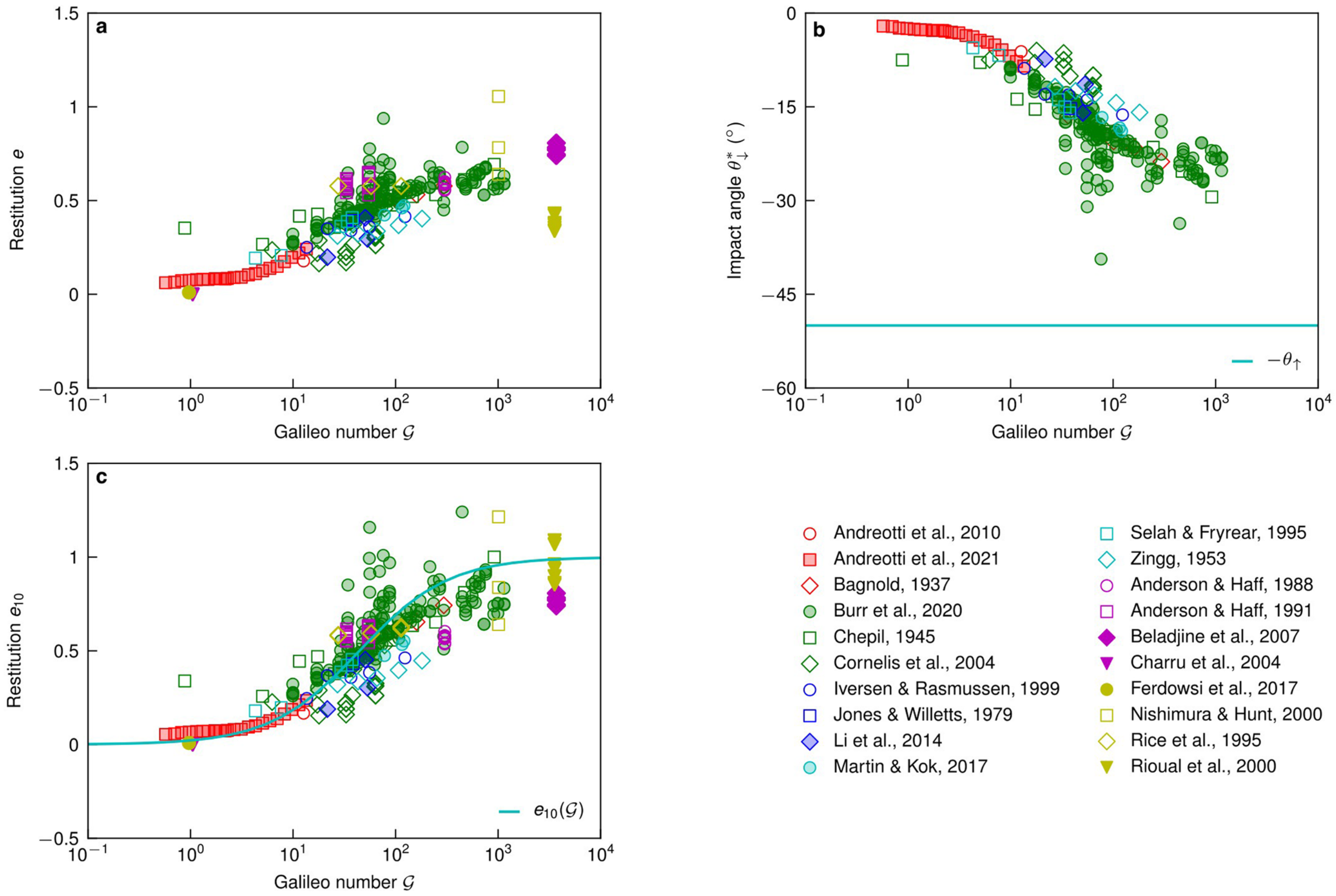

Extended Data Fig. 4 | Restitution mechanics and empirical fit. References for the observations are given on the bottom right, where markers with shaded interiors signify experiments not using standard Earth conditions or field data, markers with solid interiors signify explicit measurements of the restitution coefficients outside wind tunnels. Magenta and yellow markers are from studies where the restitution coefficient is measured or noted, values for the vertical-axes of markers with other colors are inferred from simulated trajectories. All horizontal-axes are the Galileo number $\mathcal{G}$. **(a)** The ratio of the ejection to impact velocity of a characteristic saltating grain, that is the restitution coefficient e. **(b)** The angle the grain impacts the bed, with the theoretical fixed ejection angle denoted (cyan line). **(c)** The restitution coefficient normalized such that it impacted the bed at a fixed angle ($\theta_\downarrow = -10^\circ$), e_{10}, with the empirical relationship used in the main text relating the two axes (cyan line) (Methods).

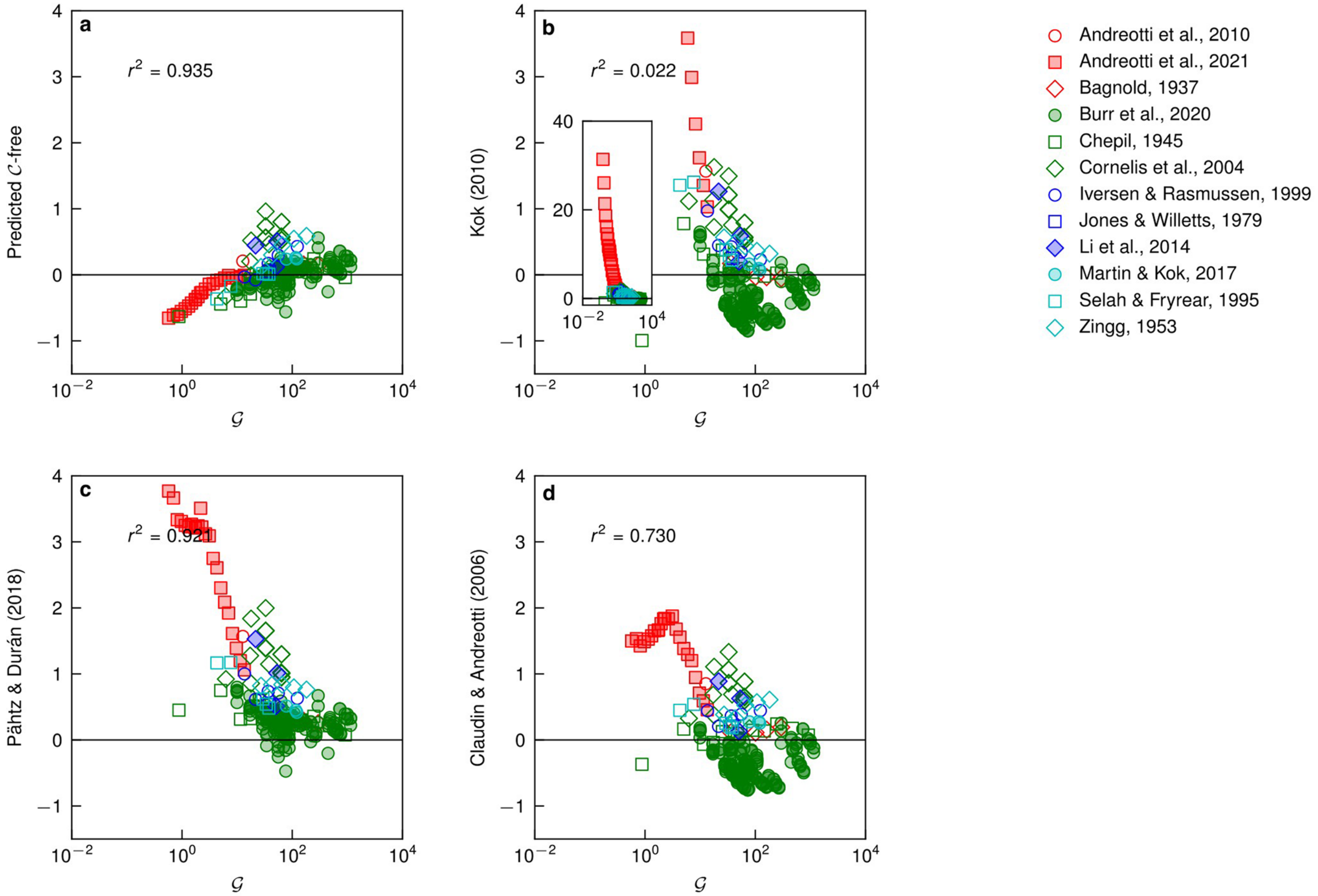

Extended Data Fig. 5 | Impact threshold prediction comparison to data. Four methods for predicting the impact threshold are compared to observed data, where the vertical axis is $u_{*,observed}/u_{*,predicted}-1$ (for the labelled prediction) and the horizontal axis is the Galileo number, $\mathcal{G}$. References for the observations are given on the right, where markers with shaded interiors signify experiments not using standard Earth conditions or field data. The correlation coefficient (r^2) for each log-log comparison of $u_{*,observed}$ versus is $u_{*,predicted}$ (that is Fig. 3c) is annotated. **(a)** The prediction in the main text. **(b)** The prediction using the semiempirical theory of Kok (2010) (note: the vertical axis bounds are extended in the inset to show the full data extent). **(c)** The prediction using the semiempirical theory of Pähtz & Durán (2018). **(d)** The prediction using the semiempirical theory of Claudin & Andreotti (2006).

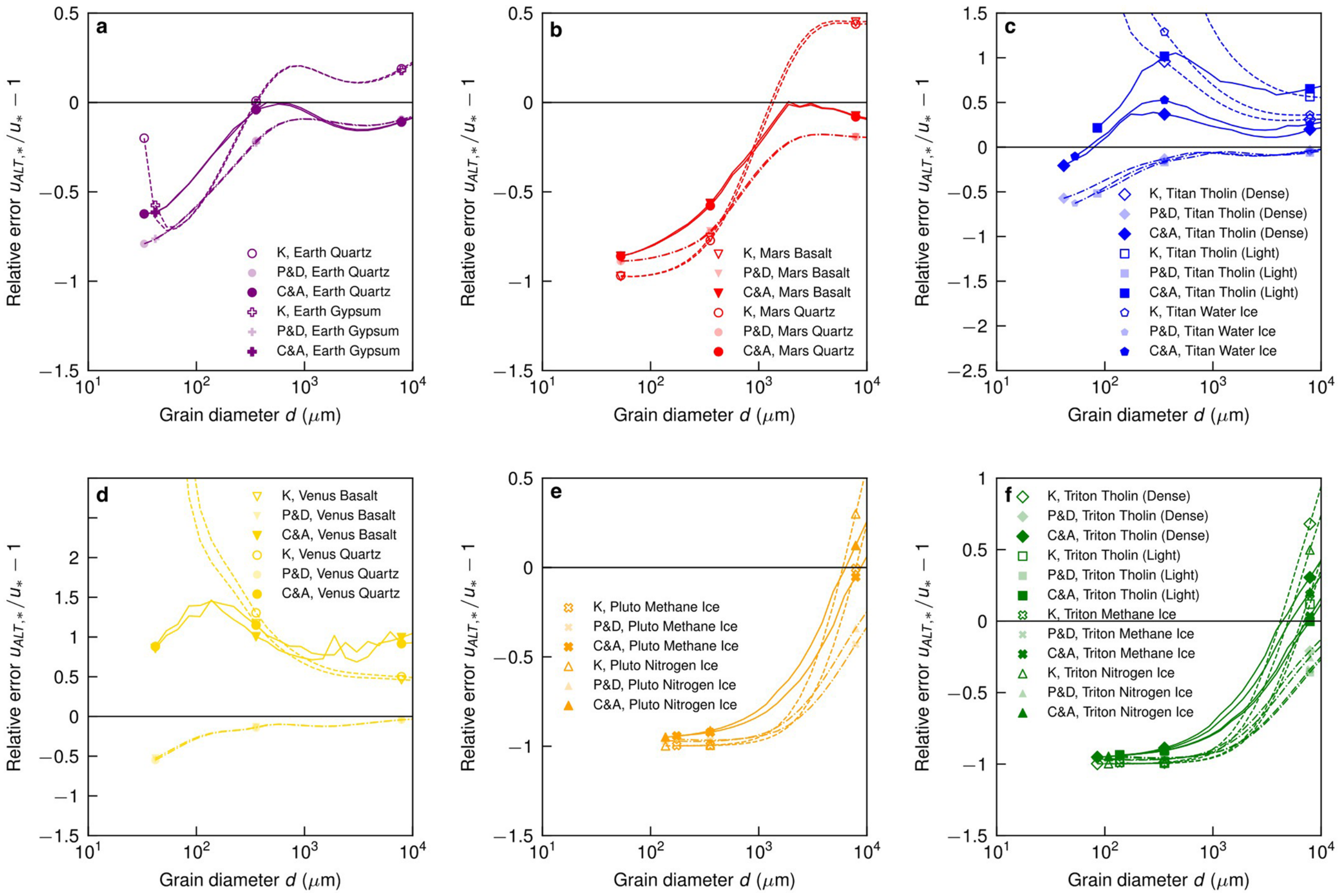

Extended Data Fig. 6 | Impact threshold prediction comparison to each other. The relative error between the alternative predictions of Kok (2010) (K), Pähtz & Durán (2018) (P&D) and Claudin & Andreotti (2006) (C&A) with the prediction in the main text for the impact threshold for average conditions on each body. Each sediment candidate is given for **(a)** Earth, **(b)** Mars, **(c)** Titan, **(d)** Venus, **(e)** Pluto and **(f)** Triton.

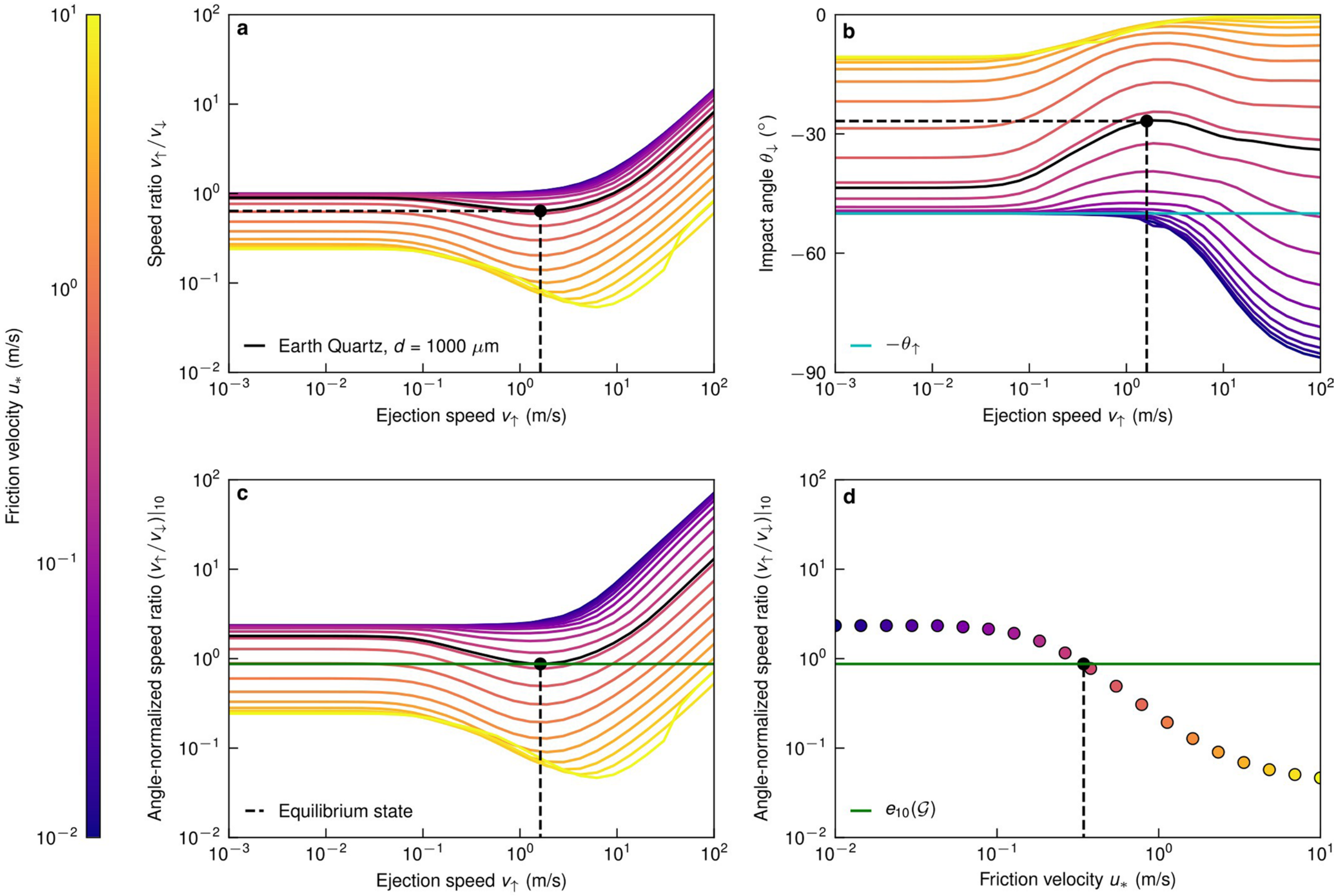

Extended Data Fig. 7 | Trajectory analysis example. (a-c) Each point on the lines with color corresponding to the colorbar on the left are for a trajectory of a 1 mm quartz grain at average Earth conditions leaving the bed with an ejection velocity of $v_\uparrow$ from the horizontal axis. The solid black line denotes the impact threshold friction velocity, while the black dot and the corresponding dashed black lines denote the unique pair of the friction velocity and ejection velocity at the impact threshold. **(a)** The ratio of the ejection to impact speeds for a trajectory. **(b)** The impact angle for a trajectory, with the cyan line indicating the ejection angle. **(c)** The ratio of the ejection to impact speeds for a trajectory, normalized as if the impact angle was fixed ($\theta_\downarrow = -10^\circ$), e_{10} (Methods). The green line (also in (d)) is the 'target' restitution coefficient for this case using the empirical relation found in Extended Data Figure 4c. **(d)** The minima for each line in (c) plotted against the friction velocity. We define the impact threshold as the intersection of the trend and the green line.

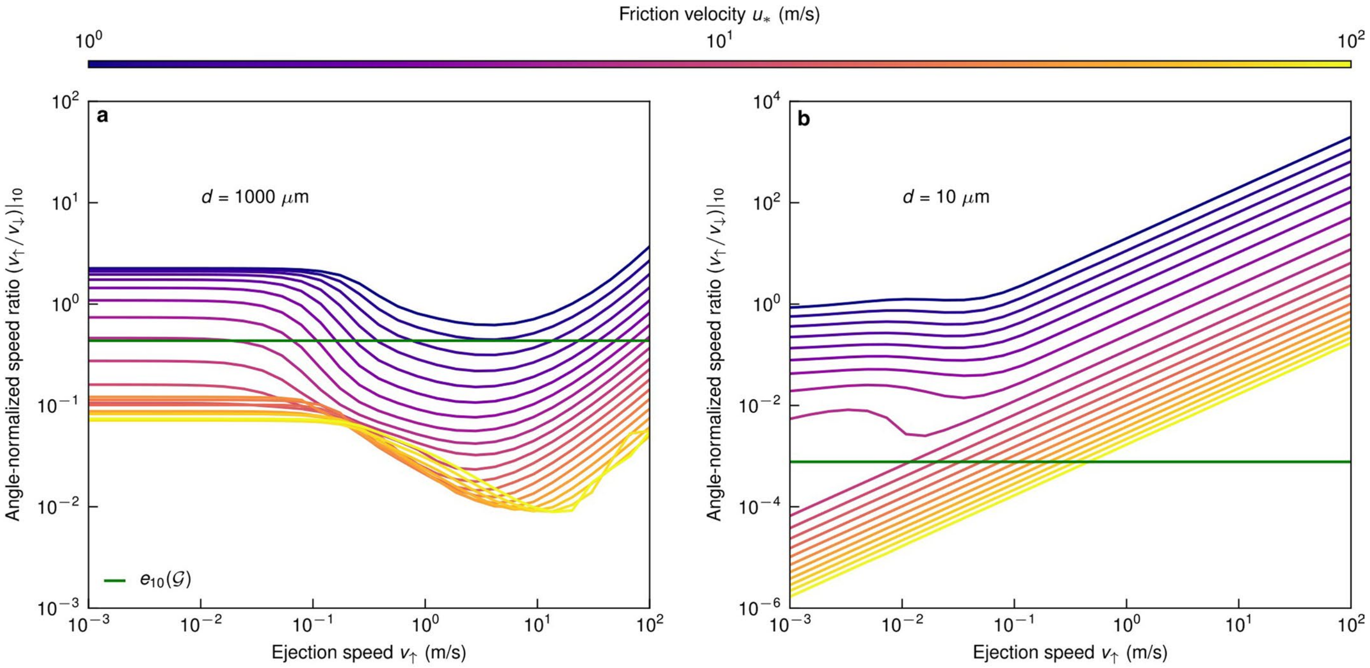

Extended Data Fig. 8 | Contrasting trajectory examples. Trajectories like Extended Data Figure 7c for Basalt grains at average Mars conditions of size **(a)** $d=1$ mm and **(b)** $d=10\mu$m. The green lines are the 'target' restitution coefficient for each case using the empirical relation found in Extended Data Figure 4c. The qualitatively different behavior in the neighborhood of the solution shows how this formulation of the impact threshold loses meaning for small grains. The minima for each successive curve of fixed friction velocity in (a) are close and transition smoothly, and u_* and $v_\uparrow$ are not extremely different. This is in contrast with (b), where the minima close to the target restitution rapidly diverges as u_* changes, and $v_\uparrow$ is extremely small at the minima relative to u_*.

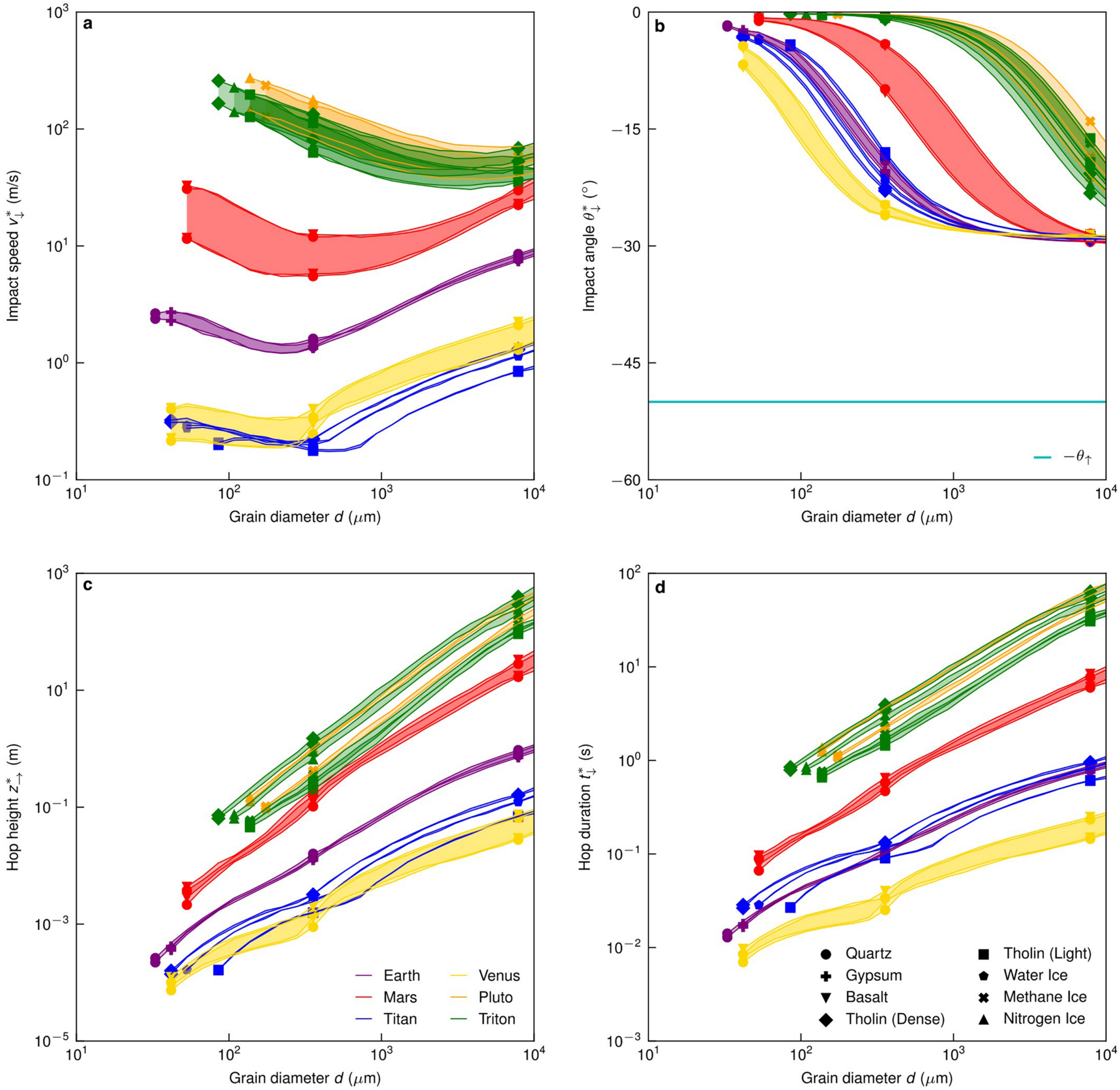

Extended Data Fig. 9 | Trajectory diagnostics. Predictions for the characteristic saltator trajectory at the impact threshold with varying grain diameter for **(a)** impact speed, **(b)** impact angle, **(c)** hop height and **(d)** hop duration. Bands show the range for different candidate and known sediments on each planetary body (see legends in (c) and (d)) based on known temperature and pressure variability.